PAPER

Check for updates

How do layered double hydroxides evolve? First *in situ* insights into their synthesis processes†

G. Doungmo, [ID] [ab] A. F. Morais, [ID] [c] D. Mustafa, [ID] [c] T. Kamgaing, [ID] [b] E. Njanja, [ID] [b] M. Etter, [ID] [d] I. K. Tonlé [ID] *[b] and H. Terraschke [ID] *[a]

Despite the importance of layered double hydroxides (LDHs) in catalysis, medicine and water treatment, the crystallisation process of these materials is seldom investigated. In this study, *in situ* characterisation techniques granted unprecedented experimental access to the formation dynamics of carbonate-intercalated Mg^{2+}/Al^{3+} LDHs as model system when applying the most relevant co-precipitation approaches by exploring the effects of temperature and concentration of reactants. For this purpose, a combinatorial multi-modal characterisation approach was applied involving *in situ* measurements of pH, ion conductivity and light scattering, as well as synchrotron-based *in situ* X-ray diffraction (XRD). Shortly after beginning the addition of basic solutions (*i.e.*, sodium carbonate and sodium hydroxide) to the solutions of magnesium nitrate hexahydrate and aluminium nitrate nonahydrate, a stable pH was reached due to the uptake of hydroxyl ions for nuclei formation. Shortly after, crystal growth phase was detected by an increase in the light scattering signal and confirmed *via in situ* XRD. Increasing the concentration of reactants accelerated the onset of crystal growth by 70% without significantly changing the crystallite size. On the other hand, increasing the temperature up to 65 °C showed a smaller influence on the reaction kinetics but resulted in a two-fold increase in crystallite size. Adding the solution of metal precursors to the basic solution, saturation was rapidly reached, without an induction period, favouring the formation of very small crystallites of approximately 10 nm.

1. Introduction

Layered double hydroxides (LDHs), also known as anionic clays or hydrotalcite-like compounds, are an important class of ionic lamellar solids.[1] Structurally, LDHs consist of positively charged metal hydroxide sheets that are intercalated by anions and water molecules.[2] The general chemical formula of these lamellar solids can be expressed as $[M_{1-x}^{2+}M_x^{3+}(OH)_2]^{x+}[(A^{n-})_{x/n} \cdot yH_2O]$ (abbreviated as $M_{1-x}^{2+}M_x^{3+}$–A), where $M^{2+/3+}$ are the divalent/trivalent metal cations within the brucite-like layers and A^{n-} are the charge-balancing anions.[3] The identities of M^{2+}, M^{3+} and A^{n-} can be varied over a wide range of possibilities, giving rise to a large class of multi-functional materials with potential applications in catalysis,[4a] drug delivery,[4b] environmental remediation,[4c] ion exchange,[4d] *etc.*

A variety of methods, including co-precipitation,[5a,b] ion exchange[5c] and the reconstruction of LDHs from calcined precursors,[5d] have been reported for the synthesis of LDHs. Co-precipitation is the simplest, least expensive and most utilised technique. Briefly, an aqueous solution with the metal precursor salts and a basic solution with the interlayer anion to be incorporated into the LDH are used. Typically applied M^{2+}/M^{3+} metals are Mg^{2+}, Fe^{2+}, Co^{2+}, Cu^{2+}, Ni^{2+}, Zn^{2+}, Al^{3+}, Cr^{3+}, Ga^{3+}, In^{3+}, Mn^{3+} and Fe^{3+}.[3a,6] Examples of interlayer anions are F^-, Cl^-, Br^-, CO_3^{2-}, NO_3^-, SO_4^{2-}, MnO_4^-, $V_{10}O_{28}^{6-}$ and $Mo_7O_{24}^{6-}$.[7]

Co-precipitation for LDH formation can be employed under high and low supersaturation conditions. Co-precipitation at low supersaturation conditions involves one of two approaches: (i) the basic solution containing the desired interlayer anion is slowly transferred into a vessel containing the solution with the metal precursors;[8] (ii) the solution with the metal precursors and the basic solution are simultaneously transferred into the reaction vessel containing water. In the latter case, the basic solution is also used to regulate and maintain a desired pH.[9] Co-precipitation at high supersaturation conditions involves the addition of the solution with the metal precursors into the basic solution.[10]

In situ characterisation techniques are important for gaining insights on the effects of crucial reaction parameters on the

[a]Institut für Anorganische Chemie, Christian-Albrechts-Universität zu Kiel, Max Eyth-Str. 2, 24118 Kiel, Germany. E-mail: hterraschke@ac.uni-kiel.de

[b]Research Unit of Noxious Chemistry and Environmental Engineering, Department of Chemistry, Faculty of Science University of Dschang, P.O. Box 67, Dschang, Cameroon. E-mail: ignas.tonle@univ-dschang.org

[c]Instituto de Física da Universidade de São Paulo, São Paulo 05508-090, Brazil

[d]Deutsches Elektronen-Synchrotron (DESY), Notkestr. 85, 22607 Hamburg, Germany

† Electronic supplementary information (ESI) available: Details of the experimental setup, *ex situ* FITR and XRD results. See DOI: https://doi.org/10.1039/d2ra05269e

formation of a targeted product; and for obtaining real-time information on the processes involved in the nucleation and crystal growth of solid materials. This allows a better control over the crystallisation process and endowment of the desired structure-related properties of the synthesised materials.[11] *In situ* characterisation techniques have been extensively applied for studying the formation of metal–organic frameworks,[12] luminescent complexes,[11a,b] quantum dots,[13] thiostanates,[14] *etc.* Their application in the synthesis of LDHs is limited almost exclusively to their post-synthetic modifications. One example is the application of *in situ* diffuse reflectance infrared Fourier-transform spectroscopy for investigating the changes of the functional groups in LDH during the intercalation of organic molecules such as (1-[2S]-3-mercapto-2-methylpropionyl)-L-proline and 4-vinylbenzenesulfonate.[15] Other important examples are time-resolved *in situ* energy-dispersive X-ray diffraction (XRD)[16] and *in situ* high-temperature XRD studies for monitoring the post-synthetic structural evolution of LDHs during thermal treatments.[17]

In the present study, we investigated the formation of $Mg_{0.75}Al_{0.25}–CO_3^{2-}$ LDH by applying *in situ* measurements of pH, ion conductivity, light scattering and synchrotron-based XRD. This combinatorial multi-modal approach is important for acquiring fundamental insights into the crystallisation processes of the LDHs at low and high supersaturation regimes as well as understanding the effects of temperature and precursor concentration on LDH nucleation and growth. To the best of our knowledge, this is the first study to report an *in situ* investigation of the formation processes of LDHs during synthesis.

2. Experimental

2.1. Materials

Magnesium nitrate hexahydrate ($Mg(NO_3)_2 \cdot 6H_2O$, 99.999%), aluminium nitrate nonahydrate ($Al(NO_3)_3 \cdot 9H_2O$, 99.997%), sodium hydroxide (NaOH, 97%), sodium carbonate (Na_2CO_3, 99.99%), iron(II) sulphate heptahydrate ($FeSO_4 \cdot 7H_2O$ 99.0%) and sulphuric acid (H_2SO_4, 99.999%) were purchased from Sigma-Aldrich (Darmstadt, Germany). All the chemicals were used without further purification.

2.2. Synthesis procedures

2.2.1. Approach A: dosing the basic solution into the metal precursor solution. In approach A (Fig. S1, ESI†), 15 mL of an aqueous Na_2CO_3 and NaOH solution (Na_2CO_3 : NaOH ratio 1 : 10) were added to the reaction vessel containing the aqueous solution of $Mg(NO_3)_2 \cdot 6H_2O$ and $Al(NO_3)_3 \cdot 9H_2O$. The concentrations, volumes, dosing rates and temperatures used for each experiment are summarised in Table 1. Following co-precipitation, the reaction solution was aged. This treatment was applied to samples S^{1X}, Ag–$S^{1x–3X}$ and Ag–$S^{40–65°C}$. Sample S^{1X} was aged at room temperature (RT) for 24 h.[18] The abbreviation "Ag" in some sample names indicates an alternative aging step performed at 65 °C for 1 h. The abbreviations "1×", "2×" and "3×" represent the increases in the concentrations of the reactants, for instance, by a factor of 1, 2 and 3, respectively, while the superscripted values "40 °C" and "65 °C" indicate the additionally applied reaction temperatures.

2.2.2. Approach B: dosing the metal precursor solution into a pH-controlled basic solution. In approach B (Fig. S1†), the metal precursor solution was dosed into the reaction vessel at a rate of 0.5 mL min^{-1} and the basic solution was dosed automatically to maintain a target pH of 10 (experiment S^B, Table 1). After dosing, an aging step at RT for 24 h was conducted.

2.2.3. Approach C: dosing the metal solution into the basic solution with no pH control. In approach C (Fig. S1†), the metal precursor solution was dosed into the solution containing Na_2CO_3 and NaOH (experiment S^C, Table 1). After dosing, an aging step at 65 °C for 1 h was performed.

2.2.4. Washing step. For all the syntheses conducted, the final solutions were centrifuged and the solid LDH materials were washed with deionised water until the pH of the filtrate was neutral and no NO_3^- ions were detected during the brown ring test.[19] This test was performed by adding 25 mg of iron(II) sulphate to 15 mL of the filtrate, followed by the slow addition of approximately 3 mL of concentrated sulphuric acid. After 1 h, a brown ring would form in the solution if NO_3^- ions are present (Fig. S2†). After washing, the solid products were dried at 90 °C for 24 h.

Table 1 Experimental conditions for the synthesis of $Mg_{0.75}Al_{0.25}–CO_3^{2-}$ LDHs

Sample ID	S^{1X}	Ag–S^{1X}	Ag–S^{2X}	Ag–S^{3X}	Ag–$S^{40°C}$	Ag–$S^{65°C}$	S^B	S^C
Approach	A	A	A	A	A	A	B	C
Measurement set-up	I	II	I	I	I	I	II	I
NaOH concentration (mol L^{-1})	0.2	0.2	0.4	0.6	0.2	0.2	0.2	0.2
Na_2CO_3 concentration (mol L^{-1})	0.02	0.02	0.04	0.06	0.02	0.02	0.02	0.02
Volume of basic solution (mL)	15	15	15	15	15	15	36.3	25
Volume of metal precursor solution (mL)	30	30	30	30	30	30	50	25
$Mg(NO_3)_2 \cdot 6H_2O$ concentration (mol L^{-1})	0.06	0.06	0.12	0.18	0.06	0.06	0.06	0.06
$Al(NO_3)_3 \cdot 9H_2O$ concentration (mol L^{-1})	0.02	0.02	0.04	0.06	0.02	0.02	0.02	0.02
Reaction temperature (°C)	25	25	25	25	40	65	25	25
Addition rate in (mL min^{-1})	0.5	0.5	0.5	0.5	0.5	0.5	0.5	0.5
Aging temperature (°C)	RT	65	65	65	65	65	RT	65
Aging time (h)	24	1	1	1	1	1	24	1

2.3. Characterisation

2.3.1. Set-up I. Set-up I included an *in situ* crystallisation cell (Mettler Toledo GmbH, Gießen, Germany, Fig. S3†) that allowed the automatic control of temperature, stirring and dosing. *In situ* measurements of pH and ion conductivity were also possible. For the measurements of *in situ* light scattering,[20] a light source (365 nm, Sahlmann Photochemical Solutions, Germany) was positioned outside the reaction vessel and the scattered light was collected using an optical fibre submersed in the reaction solution and coupled to a Fluorolog-3 spectrometer FL322 (HORIBA Jobin Yvon GmbH, Unterhaching, Germany) equipped with a Syncerity CCD detector, a R928P Photomultiplier and an iHR-320-FA triple grating imaging spectrograph. Set-up I was used in the investigations involving samples S^{1X}, $Ag{-}S^{2X}$, $Ag{-}S^{3X}$, $Ag{-}S^{40°C}$, $Ag{-}S^{65°C}$ and S^B.

2.3.2. Set-up II. Set-up II includes a Metrohm AG Titrando dosing unit (Filderstadt, Germany, Fig. S3†) coupled to the *in situ* measurements of pH and light scattering. Light scattering measurements were performed using a 365 nm light source and an optical fibre submersed in the contents of the reaction vessel, connected to a portable EPP2000 spectrometer (StellarNet Inc., United States) equipped with a CCD-based detector. *In situ* XRD measurements (60 keV) were performed at the P02.1 PETRA III beamline (Fig. S4†)[21] at the Deutsches Elektronen-Synchrotron (DESY, Hamburg, Germany) using a XRD1621 detector (2048 × 2048 pixels, 200 μm pixel size, PerkinElmer Technologies, Walluf, Germany). As explained in detail in our previous studies,[22] a glass reaction vessel was adapted with a concave cavity on one of its walls to decrease the path length of the X-ray beam through the reaction volume. The glass vessel was placed in a reactor holder equipped with an integrated stirring system designed to flexibly fit on different beamlines without requiring realignment after each reaction. In the reactor holder, two openings allowed for the passage of the X-ray beam and ultraviolet light. The temperature of the reaction solution was controlled using a LR 316 unit (JUMO GmbH & Co. KG, Germany). Set-up II was used in the investigations involving samples $Ag{-}S^{1X}$ and S^C. For clarity, the *in situ* XRD data was treated following the method suggested by Platero-Prats *et al.*[23] regarding the *in situ* pair-distribution function measurements. Thus, our *in situ* XRD data were normalised to overcome the oscillation of the intensity of the synchrotron X-ray beam. A first measurement was performed, prior to mixing the precursor solutions, as a baseline for subtracting the background caused by the reactor walls and solvent.[24]

2.3.3. *Ex situ* characterisation of powder samples. *Ex situ* XRD patterns were collected using a STOE Stadi-p X-ray powder diffractometer (STOE & Cie GmbH, Darmstadt, Germany) using $CuK_{\alpha1}$ radiation ($\lambda = 1.54056$ Å, Ge monochromator) in transmission geometry with a DECTRIS® MYTHEN 1K detector (DECTRIS, Baden-Daettwil, Switzerland). The *ex situ* XRD patterns were used to estimate the crystallite size (D) along a $[hkl]$ crystal direction through the following form of the Scherrer equation:

$$D = \frac{0.9\,\lambda}{\delta(2\theta)\cos\theta},\tag{1}$$

where θ and $\delta(2\theta)$ are, respectively, the position and the full width at half maximum of the (hkl) Bragg reflection observed in the PXRD pattern of the concerned sample and $\lambda = 1.5418$ Å is the CuK_{α} wavelength. Fourier-transform infrared (FTIR) spectroscopy was performed on a Genesis FTIRTM spectrometer (ATI Mattson) equipped with a DTGS (deuterated triglycine sulphate) detector operating in transmission mode in the spectral range from 400 to 4000 cm^{-1}. The reflection spectra were recorded at room temperature with a Varian Techtron Pty UV/Vis/NIR two-channel Cary 5000 spectrometer, using $BaSO_4$ as a reference material. Thermogravimetric analysis was performed using a Linseis STA PT1600 simultaneous thermobalance, the samples were heated in a nitrogen atmosphere at a rate of 4 K min^{-1}. In addition, the samples were analysed using a 300 kV Tecnai G2 F30 S-TWIN field emission gun (FEG) transmission electron microscope, equipped with a Si/Li energy-dispersive X-ray spectroscopy detector.

3. Results and discussion

3.1. Co-precipitation under low supersaturation conditions

3.1.1. Approach A: dosing the base into the metal precursor solution. Fig. 1a shows the time evolution of pH, the intensity of scattered light and the total volume of the basic solution dosed into the reactor during the synthesis of sample S^{1X}. The addition of the basic solution caused an increase in the pH during the early stages of the synthesis. However, the pH did not continue to increase at a rate similar to that of the addition of the basic solution, which is expected for OH$^-$ uptake by the LDH product. Additionally, a pH decrease was observed at the end of dosing process, indicating the continuation of the reaction even after the dosing had been halted. These findings are in accordance with the *in situ* light scattering measurements. In the early stages of the synthesis, the intensity of scattered light did not significantly change, suggesting that no particle or only small nuclei are present in the suspension.[25] After approximately $t = 18$ min, the pH reached 8.7 and the intensity of the scattered light started to decrease. This occurred due to crystal growth, which caused turbidity to increase beause of the appearance of big particles that obstruct the passage of light through the solution.[11c] After approximately $t = 50$ min, the pH and scattered light intensity nearly reached plateaus.

The formation of carbonate-intercalated $Mg_{0.75}Al_{0.25}{-}CO_3{}^{2-}$ LDHs *via* Approach A was confirmed using *ex situ* powder X-ray diffraction (PXRD). Fig. 1b shows the PXRD pattern of sample S^{1X}, which has been indexed based on a 3-layer hexagonal unit cell to facilitate comparison with LDHs in the literature.[2a,b,26] At 11.47° 2θ, the Bragg reflection observed is related to the basal spacing c_0 of sample S^{1X}. A value of $c_0 = d_{(003)} = 7.6$ Å, typical of LDHs interspersed by carbonate ions,[27] can be calculated using Bragg's law. The Bragg peak around 60.6° 2θ corresponded to the (110) reflection, whose interplanar spacing ($d_{(110)} = 1.53$ Å) was used to calculate the intermetallic distance (a_{MM}) within the hydroxide layers ($a_{MM} = 2d_{(110)} = 3.06$ Å).[26] The full width at half maximum (FWHM) of the (003) Bragg reflection was $\delta(2\theta) = 0.8°$; therefore, the average crystallite size in the stacking
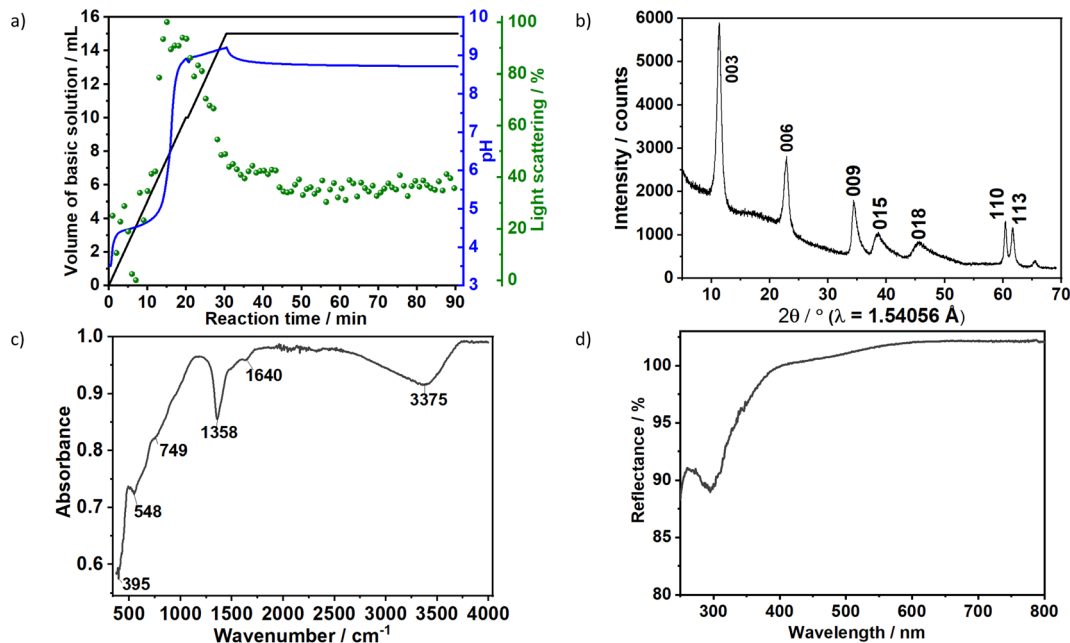
Fig. 1 (a) Time dependence of the scattered light intensity at 365 nm (green), pH (blue) and dosed volume of the basic solution (black) during the synthesis of sample S^{1X}. *Ex situ* (b) XRD pattern, (c) FTIR spectrum and (d) UV/vis reflection spectroscopy.

direction was estimated to be 15.4 nm, corresponding to the stacking of 20 hydroxide layer slabs in average.

Characteristic vibrations on the IR spectrum of sample S^{1X} (Fig. 1c) further indicated LDH formation. The strong broad absorbance band between 3000 and 3500 cm^{-1} corresponded to the stretching vibration of hydrogen-bonded hydroxyl groups from the hydroxide layers and interlayer water.[27,28] The weak band observed at approximately 1640 cm^{-1} was attributed to the bending mode of H$_2$O.[29] IR absorptions at 749, 1358 and 548 cm^{-1} reflect the ν_2, ν_3 and ν_4 stretching vibrations of interlayer CO$_3^{2-}$ anions. In the low energy range, the band located at approximately 395 cm^{-1} was attributed to the vibrations of O–M$^{2+/3+}$–O, Mg–OH and Al–OH in the hydroxide layers.[30] No additional band was observed between 1390 and 1425 cm^{-1}, indicating that NO$_3^-$ ions from the metal precursors were successfully substituted by CO$_3^{2-}$ ions.[30] Ultraviolet-Visible reflectance spectroscopy (Fig. 1d) showed that the formed LDH reflects nearly 100% of the light in the visible range. For wavelengths below 400 nm, the reflectance decreased,

indicating an increase in optical absorbance in this area, with the highest absorbance observed at approximately 300 nm.

The very thin aspect of the layer slabs was confirmed by transmission electron microscopy (Fig. 2a), which revealed that sample S^{1X} is composed by extremely thin flakes extended between approximately 30 nm and 100 nm. Energy-dispersive X-ray spectroscopy (Fig. 2b) confirmed the S^{1X} composition containing the Mg/Al ratio of 3 : 1, besides C and O. Even though the sample morphology remained unchanged, the exposition to the electron beam caused the decomposition of the CO$_3^{2-}$ anions, indicated by the low C concentration as well as the partial conversion of S^{1X} to MgO, shown by the electron diffraction patterns (Fig. 2b, inset).

Thermal analyses revealed two main endothermic peaks in the intervals 150–250 °C and 250–450 °C, observed during the thermal decomposition of the sample S^{1X} (Fig. 2c). The first peak occurs due to the loss of water molecules contained in the interlayer space. The peak at 400 °C contain a shoulder at 370 °C, attributed in the literature to the loss of hydroxyl groups
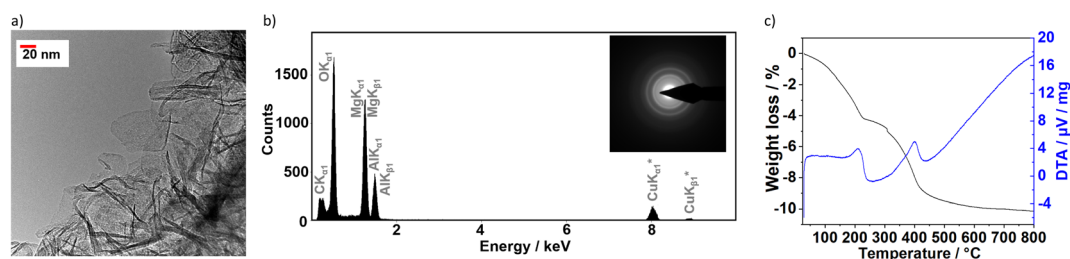

Fig. 2 (a) TEM image, (b) EDX results, electron diffraction pattern (inset), (c) thermogravimetric and differential thermal analyses of Sample S^{1X}. The asterisks (*) identify the Cu signal from the TEM grid.
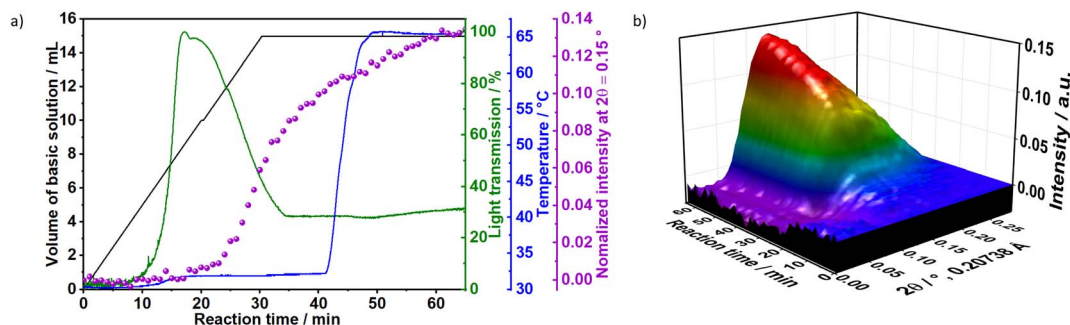
Fig. 3 (a) *In situ* measurements of light scattering at 375 nm (green), temperature (blue), normalised XRD intensity at $2\theta = 0.15°$ (purple) and volume of the basic solution dosed into the reaction vessel (black). (b) *In situ* XRD during the synthesis of sample Ag–S^{1X} (synchrotron radiation, $\lambda = 0.20738$ Å, 60 keV).

bound to Al, while the main peak at 400 °C is generated by the loss of hydroxyl groups bound to Mg together with the removal of intercalated carbonate anions.[31]

To gain additional insight on the time evolution of LDH formation, *in situ* XRD and light scattering measurements were simultaneously performed during the synthesis of sample Ag–S^{1X} (set-up II at DESY, Fig. 3a), synthesised under similar conditions as those used for obtaining sample S^{1X}. Similar to S^{1X}, the plateau observed for the green curve at $t < 10$ min suggests the formation of nuclei that are too small to scatter the 365 nm green light,[25] which is in-line with the plateau observed during the *in situ* pH measurements (Fig. 1a). At approximately $t = 10$ min, 4 mL of the basic solution have been dosed into the metal precursor solution, the synthesis solution became heterogeneous and a steep increase in the scattered light intensity is observed. During the synchrotron-based *in situ* XRD measurements, the background of the small-angle range (0.15° 2θ) started to increase. This result was assigned to the formation low-crystallinity materials, such as amorphous compounds or nanoparticles,[32] in accordance with the increase of light scattering in this reaction period. The low crystallinity of the product was also indicated by the broad Bragg reflections of the synthesised LDHs in the XRD pattern in Fig. 1b. At approximately $t = 20$–25 min, both a steep increase in the small-angle signal (Fig. 3b) and drastic decrease in the scattered light intensity (Fig. 3a) were observed, indicating the further growth of the LDH crystallites. The decrease in light scattering after approximately $t = 20$ min can be explained by the increase in turbidity caused by the crystal growth, until reaching saturation at approximately $t = 34$ min. The increase in temperature to 65 °C at approximately $t = 42$ min did not significantly affect product formation as suggested by the *in situ* XRD measurements.

3.1.1.1 Influence of the concentrations of reactants. To evaluate the influence of the concentration of reactants on the crystallisation of LDHs, the results for samples Ag–S^{2X} and Ag–S^{3X} were analysed simultaneously (Fig. 4). These samples respectively correspond to a 2-fold and 3-fold increase in the concentration of the basic solution and metal precursor solution in comparison with sample Ag–S^{1X}. The increase in concentration caused the initiation of the nucleation and growth processes earlier, as seen from the scattered light

intensity, which started to increase over shorter time intervals for Ag–S^{2X} and Ag–S^{3X} in comparison with S^{1X} and Ag–S^{1X}. This feature is explained by the faster achievement of the critical saturation level when the reactants are dosed at higher concentrations. Moreover, the maximum scattered light intensity occurs at approximately 20, 12 and 6 min for S^{1X}, Ag–S^{2X} and Ag–S^{3X}, respectively, inversely following the 1 : 2 : 3 scaling of the reactant concentrations. Apart from the shorter raising time of the scattered light intensity curves, this inverse scaling is expected from a nucleation process that only starts after a particular critical supersaturation level is achieved.

After 90 min of reaction, the temperature was raised from room temperature to 65 °C. For Ag–S^{2X} (Fig. 4), this led to
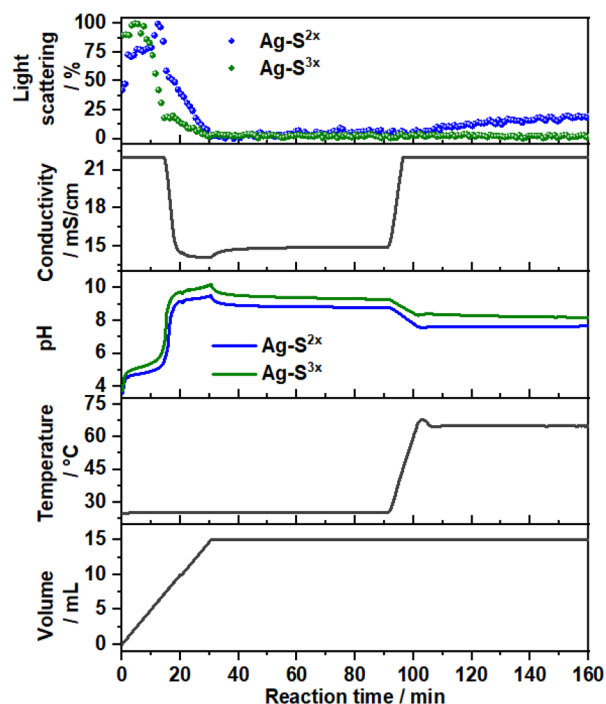

Fig. 4 Time evolution of *in situ* light scattering at 365 nm, ion conductivity, pH, temperature (magenta) and dosed volume of the basic solution obtained during the synthesis of the samples Ag–S^{2X} and Ag–S^{3X}. Measurements of ion conductivity during the synthesis of Ag–S^{2X} at $t < 12$ min and $t > 95$ min were saturated.

a decrease in the turbidity of the suspension as indicated by the scattered light intensity curve, implying the initiation of Ostwald ripening *via* the dissolution of small particles in the suspension. *In situ* measurements of ion conductivity of the solution have confirmed the intense crystal growth at approximately $t = 12$ min. Before this period, the curve was strongly saturated, while the conductivity sharply decreased afterwards due to the uptake of ions from the solution for further growth of the LDH. In accordance with the *in situ* pH (Fig. 1 and 3) and *in situ* XRD (Fig. 3) measurements, the conductivity changes slightly after finishing the dosing process, indicating that the reaction has not reached completion.

Interestingly, samples Ag–S^{1X}, Ag–S^{2X} and Ag–S^{3X} have very similar *ex situ* XRD patterns (Fig. S5a†), which provides an easy upscaling route *via* Approach A for which higher amounts of LDHs can be produced without drastically changing the crystalline properties of the product. Indeed, the FWHM of the (003) Bragg reflections of samples Ag–S^{1X}, Ag–S^{2X} and Ag–S^{3X} were 1.67, 1.62 and 1.64° 2θ ($\lambda = 1.54060$ Å), corresponding to Scherrer crystallite sizes of 5.0, 5.2 and 5.1 nm, respectively.

3.1.1.2 Influence of reaction temperature. To evaluate the influence of the nucleation temperature (Fig. 5a) on the crystallisation of LDHs, the results for the *in situ* measurements of light scattering, ion conductivity and pH were plotted for samples S^{1X}, Ag–S$^{40°C}$ and Ag–S$^{65°C}$, which were synthesised at 25, 40 and 65 °C, respectively. In Fig. 5b, despite the high noise within the nucleation range (marked in grey), *in situ* light scattering measurements demonstrated in general the influence of the reaction temperature on LDH formation. For example, the decrease in light scattering caused by the strong turbidity resulting from LDH crystal growth started at

approximately $t = 20$ min at 25 °C, $t = 14$ min at 40 °C and $t = 11$ min at 65 °C. These results agreed with the ones obtained during the *in situ* conductivity measurements. For the reaction at 25 °C (S^{1X}), the ion conductivity decreased in two steps: The first step, until approximately $t = 13$ min, was assigned to the uptake of ions for the formation of LDH nuclei, which did not significantly influence light transmission. The second step ($t \approx$ 13–15 min) was faster and assigned to crystal growth, which caused the increase of the scattering signal because of the increased dispersion of light by the newly formed particles before causing the decrease on light scattering due to the increase on turbidity, as indicated by *in situ* XRD results (Fig. 3). Interestingly, Fig. 5c shows that after approximately $t = 20$ min, the conductivity did not change significantly, suggesting that the crystal growth occurring within this reaction period may take place in parallel with the dissolution of small particles in the suspension. Similar to the light scattering measurements, the temperature rise shortened the time in which the conductivity stopped decreasing from approximately $t = 19$ min at 25 °C, $t = 15$ min at 40 °C and $t = 13$ min for 65 °C. Fig. 5d shows that the pH also increases at different rates after approximately $t = 19$ min at 25 °C, $t = 15$ min at 40 °C and $t = 13$ min for 65 °C, confirming the influence of temperature on LDH formation.

In line with the classical nucleation theory,[33] a maximum nucleation rate is reached at a particular temperature (T_{max}), above which growth is increasingly favoured over nucleation. This effect can be partially rationalised based on the large critical size of the nucleus and the expected increase in the solubility product of the solid phase with increasing temperature. The latter leads to a decrease in the supersaturation ratio. This drastically decreases the rate of nucleation when compared
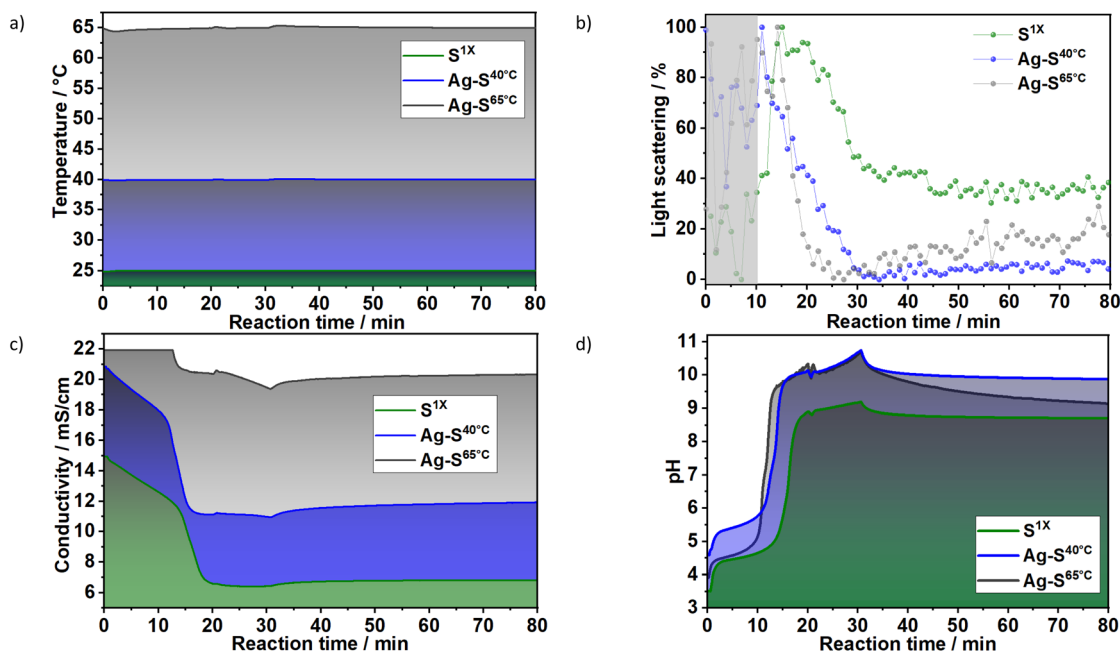

Fig. 5 *In situ* measurements of (a) temperature, (b) light scattering, (c) ionic conductivity and (d) pH value during synthesis of the samples S^{1X} (green), Ag–S$^{40°C}$ (blue) and Ag–S$^{65°C}$ (grey). The ionic conductivity values at 65 °C reached saturation for $t < 12$ min. The dosing rate of the basic to metallic solutions applied at this experiment was the same one as shown in Fig. 1–3.

with the decrease in growth rate, leading to fewer nuclei and larger particles. The effect of this on the turbidity of the solution is immediate, as the scattered intensity is known to scale with the 6th-power of the particle size.[34] Thus, the behaviour observed for the scattered light intensities obtained for S^{1X}, Ag–$S^{40°C}$ and Ag–$S^{65°C}$ (Fig. 5b) can be explained by assuming that the reaction temperatures used for these samples were above T_{max}. This assumption was further supported by recent observations by Tathod et al.,[33] indicating a T_{max} value that is lower than or approximately −15 °C.

The effect of an increased reaction temperature can also be seen in the ex situ XRD patterns of samples Ag–S^{1X}, Ag–$S^{40°C}$ and Ag–$S^{65°C}$ (Fig. S6†). With the increase in reaction/aging temperature, sharper Bragg reflections were observed, indicating an increase in crystallite dimensions in the stacking direction and hydroxide plane. Indeed, along the stacking direction, the analysis of the (003) Bragg reflections for samples Ag–S^{1X}, Ag–$S^{40°C}$ and Ag–$S^{65°C}$ gives FWHM values of 1.67, 1.27 and 0.74° 2θ ($\lambda = 1.54060$ Å), corresponding to Scherrer crystallite sizes of 5.0, 6.6 and 11.3 nm, respectively. This trend repeats in the hydroxide plane and Gaussian fittings for the (110) Bragg reflections, which gives FWHM values of 1.18, 0.89

and 0.62° 2θ for Ag–S^{1X}, Ag–$S^{40°C}$ and Ag–$S^{65°C}$, which correspond to crystallite sizes of 8.2, 10.9 and 15.5 nm, respectively.

3.1.2. Approach B: dosing the metal precursor and basic solutions at a constant pH value. Additional experiments were carried out for the in situ monitoring of LDH formation but now exploring the simultaneous addition of the metal precursor and basic solutions (approach B, Fig. S1†). In approach B, the metal precursor solution was added to the reaction vessel at a fixed rate (Table 1, Fig. 6a), while the basic solution was dosed into the vessel to maintain a target pH of approximately 10 (Fig. 6b). At this pH, the suspension started to become turbid after around $t = 3$ min, as observed in the light scattering curve (Fig. 6c). The short plateau at $t < 3$ min in the light transmission curve relates to a time before critical supersaturation is achieved and before particle growth commences. The light scattering results further revealed that the growth process continues until the dosing of the metal precursor solution is complete, with an ever-increasing turbidity of the suspension. Ex situ XRD analysis (Fig. 6d) shows the onset of LDH formation at $t = 30$ min and during the aging step at $t = 4$ h until final product formation. The formation of the LDH product for
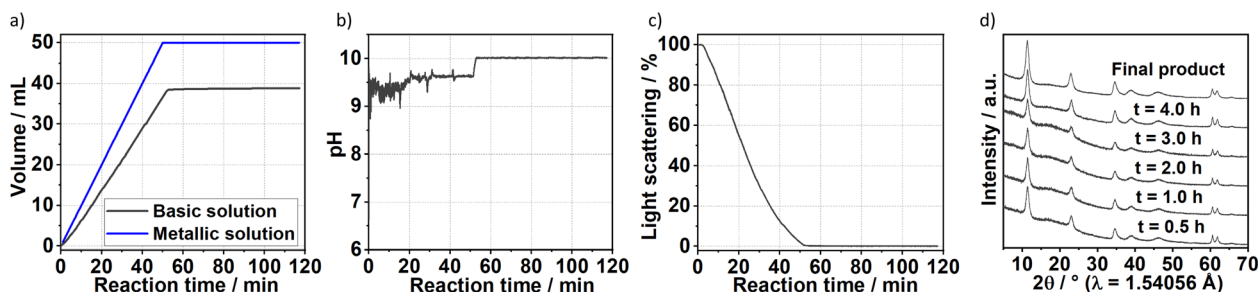

Fig. 6 Time evolution of the (a) dosed volume of the metal precursor solution (blue) and dosed volume of the basic solution (black) as well as the in situ measurements of (b) pH and (c) light scattering during the synthesis of sample S^B, with (d) ex situ XRD results obtained from aliquots removed during the aging step.
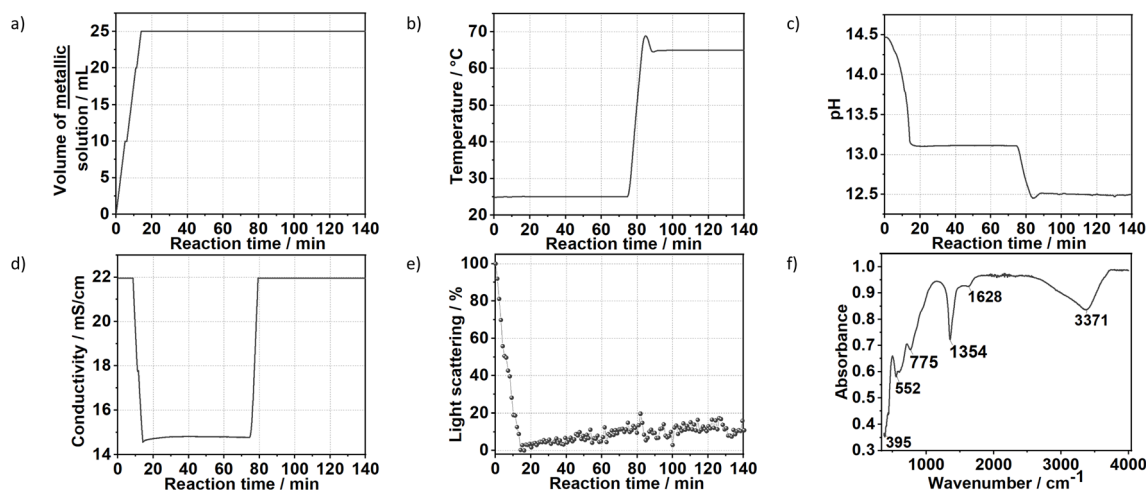

Fig. 7 Time evolution of the (a) dosing of the metal precursors solution, (b) temperature, (c) pH value, (d) conductivity, (e) light scattering during the synthesis of the sample S^C. (f) FTIR measurement of the final product. The ion conductivity measurements reached saturation at $t < 10$ min and at $t > 85$ min.

sample S^B was also supported by additional FTIR measurements (Fig. S7†).

3.2. Approach C: dosing the metal precursor solution into a concentrated NaOH solution

Fig. 7 shows the time evolution of pH, the intensity of the light scattered by the synthesis solution, ion conductivity and the dosed volume of the metal precursor solution during the formation and aging step at 65 °C of sample S^C as well as the respective FTIR results. At a high starting pH of 14.5, critical supersaturation is reached very rapidly. Indeed, no induction period is observed from the light transmission results, with the reaction solution becoming turbid from the beginning of the dosing process, as indicated by the monotonic decrease of the scattered light intensity at $t < 12$ min. Approach C produces LDHs with the sharpest (110) Bragg reflections in comparison with those of the other prepared samples. With a FWHM of 0.6°, a crystallite dimension of approximately 16 nm in the hydroxide plane of the LDHs is obtained from the Scherrer equation. Also, a high crystallinity is attained along the stacking direction, with the (003) Bragg reflection (Fig. S8†) having a FWHM of 0.8°, corresponding to a Scherrer crystallite size of approximately 10 nm. The high crystallinity of S^C is attributed to the combination of aging and a higher supersaturation rate (when compared with those of the other samples). As known from the classical nucleation theory,[33,35] higher supersaturation rates favour nucleation over crystal growth, thereby forming smaller particles by the end of the dosing. However, in the aging step, these small crystals are more likely to be dissolved by the suspension. These redissolved cations can then be recrystallised at high temperatures at a lower supersaturation ratio, which would favour crystal growth.[33] Under this mechanism, a suspension with a high fraction of small crystals would be easily converted to a suspension of highly crystalline particles during the aging step. This interpretation is further supported by the very sharp (110) and (113) Bragg reflections of sample S^C, indicating high crystallinity in the *ab*-plane of the LDHs, which is expected to benefit most from Ostwald ripening due to the higher defect density in the edges of the *ab*-planes.

4.   Conclusion

The application of *in situ* characterisation techniques granted experimental access to the crystallisation dynamics of LDHs. The nucleation process and initiation of crystal growth were both monitored *via in situ* light scattering measurements. The increase in turbidity could be correlated to the rate of crystal growth in the suspension, and in a more direct way, the appearance of the first LDH particles could be followed using synchrotron-based *in situ* XRD.

Here, three different co-precipitation procedures were investigated. When the basic solution was dosed into the metal precursor solution (approach A), crystal growth was shown to be kinetically favoured over nucleation as the reaction temperature increased, resulting in the formation of large LDH crystallites. This outcome was correlated to the rapid turbidity of the

suspension at high temperatures as the scattered intensity scales with the 6th-power of particle size.

Under an increase in the reactant concentration, the initiation of the nucleation and growth processes was brought forward because of the faster achievement of the critical supersaturation level. Under the evaluated conditions of this study, this effect had no impact on the crystalline properties of the final LDH products as observed by *ex situ* PXRD.

The pH played a vital role in determining the crystallisation kinetics of LDHs. At high pH, here exemplified by approach C (pH between 12.5 and 14.5) in contrast to approach B (pH 10), a higher supersaturation level was achieved for similar dosing rates. Higher supersaturation increasingly favours nucleation over crystal growth, leading to the formation of smaller crystals. By aging at high temperatures, these crystals then underwent Ostwald ripening, being dissolved and recrystallised at lower supersaturation and leading to the formation of LDH particles with high crystallinity.

In summary, *in situ* characterisation techniques are powerful tools for analysing how parameters such as temperature, reactant concentration and pH influence the nucleation and growth of LDHs. Careful interpretation of the experimental results, considering the classical nucleation theory, can produce a more rational understanding of how to optimise the synthesis parameters of these materials towards the desired physicochemical properties.

Conflicts of interest

There are no conflicts to declare.

Acknowledgements

References

1 (a) D. Wang, Q. Li, C. Han, Q. Lu, Z. Xing and X. Yang, *Nat. Commun.*, 2019, **10**, 3899; (b) F. Zhang, L. Zhao, H. Chen, S. Xu, D. G. Evans and X. Duan, *Angew. Chem.*, 2008, **120**, 2500; (c) P. J. Sideris, U. G. Nielsen, Z. Gan and C. P. Grey, *Science*, 2008, **321**, 113.

2 (a) A. C. Teixeira, A. F. Morais, I. G. N. Silva, E. Breynaert and D. Mustafa, *Crystals*, 2019, **153**, 1; (b) A. F. Morais, F. O. Machado, A. C. Teixeira, I. G. N. Silva, E. Breynaert and D. Mustafa, *J. Alloys Compd.*, 2019, **771**, 578; (c) C. Mousty, C. Forano, S. Fleutot and J. C. Dupin, *Electroanalysis*, 2009, **21**, 399; (d) B. Ballarin, A. Mignani, E. Scavetta, M. Giorgetti, D. Tonelli, E. Boanini, C. Mousty and V. Prevot, *Langmuir*, 2012, **28**, 15065.

3 (a) Y. Zhao, Y. Zhao, G. I. N. Waterhouse, L. Zheng, X. Cao, F. Teng, L. Z. Wu, C. H. Tung, D. O'Hare and T. Zhang, *Adv. Mater.*, 2017, **29**, 1703828; (b) S. Radha, W. Milius, J. Breu and P. V. Kamath, *Solid State Chem.*, 2013, **204**, 362; (c) J. Liu, Y. Li, X. Huang, G. Li and Z. Li, *Adv. Funct. Mater.*, 2008, **18**, 1448.

4 (a) C. G. Silva, Y. Bouizi, V. Fornés and H. García, *J. Am. Chem. Soc.*, 2009, **131**, 13833; (b) M. A. Rocha, P. A. D. Petersen, E. Teixeira-Neto, H. M. Petrilli, F. Leroux, C. Taviot-Gueho and V. R. L. Constantino, *RSC Adv.*, 2016, **6**, 16419; (c) A. Khenifi, Z. Derriche, C. Mousty, V. Prévot and C. Forano, *Appl. Clay Sci.*, 2010, **47**, 362; (d) M. Everaert, R. Warrinnier, S. Baken, J. P. Gustafsson, D. D. Vos and E. Smolders, *ACS Sustainable Chem. Eng.*, 2016, **4**, 4280.

5 (a) L. Mohapatra and K. Parida, *J. Mater. Chem. A*, 2016, **4**, 10744; (b) F. L. Theiss, G. A. Ayoko and R. L. Frost, *Appl. Surf. Sci.*, 2016, **383**, 200; (c) Y. Wang, P. Wu, B. Li, N. Zhu and Z. Dang, *Appl. Clay Sci.*, 2011, **53**, 615; (d) J. Rocha, D. M. Arco, V. Rives and M. A. Ulibarri, *J. Mater. Chem.*, 1999, **9**, 2499.

6 G. Prestopino, G. Arrabito, A. Generosi, A. Mattoccia, B. Paci, G. Perez, G. Verona-Rinati and P. G. Medaglia, *Sci. Rep.*, 2019, **19**, 11498.

7 (a) Q. Wang and D. O'Hare, *Chem. Rev.*, 2012, **112**, 4124; (b) J. Yu, Q. Wang, D. O'Hare and L. Sun, *Chem. Soc. Rev.*, 2017, **46**, 5950.

8 (a) H. Yin, L. Cui, S. Ai, H. Fan and L. Zhu, *Electrochim. Acta*, 2010, **55**, 603; (b) B.-K. Kim, G.-H. Gwak, T. Okada and J.-M. Oh, *J. Solid State Chem.*, 2018, **263**, 60.

9 (a) M. Sun, J. Su, S. Liu, D. Wang, W. Yan, L. Zhang, Y. Xiao and X. Gao, *RSC Adv.*, 2015, **5**, 80978; (b) Y. Xiao, M. Sun, L. Zhang, X. Gao, J. Su and H. Zhu, *RSC Adv.*, 2015, **5**, 28369.

10 (a) M. Yang, O. McDermott, J. C. Buffet and D. O'Hare, *RSC Adv.*, 2014, **4**, 51676; (b) C. Nyambo, P. Songtipya, E. Manias, J. M. M. Gasco and C. A. Wilkie, *J. Mater. Chem.*, 2008, **18**, 4827.

11 (a) L. Ruiz Arana, P. Lindenberg, H. Said, M. Radke, N. Heidenreich, C. S. Cunha, S. Leubner and H. Terraschke, *RSC Adv.*, 2017, **7**, 52794; (b) P. Polzin, I. V. Eliani, J. Ströh, M. Braun, N. Ruser, N. Heidenreich, P. Rönfeldt, F. Bertram, C. Näther, S. Wöhlbrandt, M. Suta and H. Terraschke, *Phys. Chem. Chem. Phys.*, 2018, **20**, 7428; (c) N. Pienack, P. Lindenberg, G. Doungmo, N. Heidenreich, F. Bertram, M. Etter, M. T. Wharmby and H. Terraschke, *Z. Anorg. Allg. Chem.*, 2018, **644**, 1902; (d) P. Lindenberg, L. Ruiz Arana, L. K. Mahnke, P. Rönfeldt, N. Heidenreich, G. Doungmo, N. Guignot, R. Bean, H. N. Chapman, D. Dierksmeyer, J. Knoska, M. Kuhn, J. Garrevoet, V. Mariani, D. Oberthuer, K. Pande, S. Stern, A. Tolstikova, T. A. White, K. R. Beyerlein and H. Terraschke, *React. Chem. Eng.*, 2019, **4**, 1757; (e) H. Terraschke, M. Rothe and P. Lindenberg, *Rev. Anal. Chem.*, 2018, **37**, 20170003.

12 (a) P. Rönfeldt, H. Reinsch, M. P. M. Poschmann, H. Terraschke and N. Stock, *Cryst. Growth Des.*, 2020, **20**, 4686; (b) P. Rönfeldt, E. S. Grape, A. K. Inge, D. V. Novikov, A. Khadiev, M. Etter, T. Rabe, J. Benecke, H. Terraschke and N. Stock, *Inorg. Chem.*, 2020, **59**, 8995.

13 (a) C. Palencia, R. Seher, J. Krohn, F. Thiel, F. Lehmkühler and H. Weller, *Nanoscale*, 2020, **12**, 22928; (b) H. Huang, M. W. Feil, S. Fuchs, T. Debnath, A. F. Richter, Y. Tong, L. Wu, Y. Wang, M. Döblinger and B. Nickel, *Chem. Mater.*, 2020, **32**, 8877.

14 (a) N. Pienack, C. Nather and W. Bensch, *Eur. J. Inorg. Chem.*, 2009, **7**, 937; (b) B. Seidlhofer, N. Pienack and W. Bensch, *Z. Naturforsch., B: J. Chem. Sci.*, 2010, **65**, 937; (c) B. Seidlhofer, E. Antonova, J. Wang, D. Schinkel and W. Bensch, *Z. Anorg. Allg. Chem.*, 2012, **638**, 2555; (d) N. Pienack and W. Bensch, *Angew. Chem., Int. Ed.*, 2011, **50**, 2014.

15 (a) H. Zhang, S. H. Guo, K. Zou and X. Duan, *Mater. Res. Bull.*, 2009, **44**, 1062; (b) D. Yan, J. Lu, M. Wei, H. Li, J. Ma, F. Li, D. G. Evans and X. Duan, *J. Phys. Chem. A*, 2008, **112**, 7671.

16 (a) F. Millange, R. I. Walton and D. J. O'Hare, *Mater. Chem.*, 2000, **10**, 1713; (b) G. R. Williams and D. O'Hare, *J. Mater. Chem.*, 2006, **16**, 3065.

17 L. H. Zhang, F. Li, D. G. Evans and X. Duan, *J. Mater. Sci.*, 2010, **45**, 3741.

18 P. Vicente, M. Perez-Bernal, R. J. Ruano-Casero, D. Ananias, P. F. A. Almeida, J. Rocha and V. Rives, *Microporous Mesoporous Mater.*, 2016, **226**, 209.

19 E. Wiberg and A. F. Holleman, *Inorganic Chemistry*, Walter de Gruyter Press, 2001, 101st edn, ISBN 0-12-352651-5.

20 (a) J. R. Guzman-Sepulveda, J. Deng, J. Y. Fang and A. Dogariu, *Soft Matter*, 2016, **12**, 5986; (b) Y. Xing, U. O. Koylu and D. E. Rosner, *Appl. Opt.*, 1999, **12**, 2686.

21 A. C. Dippel, H. P. Liermann, J. T. Delitz, P. Walter, H. S. Schrepping, O. H. Seeck and H. Franz, *J. Synchrotron Radiat.*, 2015, **22**, 675.

22 (a) J. Ströh, L. Ruiz Arana, P. Polzin, I. V. Eliani, P. Lindenberg, N. Heidenreich, C. S. Cunha, S. Leubner and H. Terraschke, *Z. Anorg. Allg. Chem.*, 2019, **645**, 537; (b) H. Terraschke, M. Rothe, A. M. Tsirigoni, P. Lindenberg, A. L. Ruiz, N. Heidenreich, F. Bertram and M. Etter, *Inorg. Chem. Front.*, 2017, **4**, 1157.

23 A. E. Platero-Prats, Z. Li, L. C. Gallington, A. W. Peters, J. T. Hupp, O. K. Farha and K. W. Chapman, *Faraday Discuss.*, 2017, **201**, 337.

24 L. Ruiz Arana, J. Ströh, J. Amtsfeld, G. Doungmo, D. Novikov, A. Khadiev, M. Etter, M. Wharmby, M. Suta and H. Terraschke, *Z. Naturforsch., B: J. Chem. Sci.*, 2022, **77**, 263.

25 H. Goesmann and C. Feldmann, *Angew. Chem., Int. Ed.*, 2010, **49**, 1362.

26 X. Duan, D. Evans, J. He, Y. Kang, A. I. Khan, F. Leroux, B. Li, F. Li, D. O'Hare, R. C. T. Slade, C. Taviot-Gueho, M. Wei and G. Williams, *Struct. Bonding*, 2006, **119**, 1.

27 M. J. D. Reis, F. Silvério, J. Tronto and J. B. J. Valim, *Phys. Chem. Solids*, 2004, **65**, 487.

28 M. R. Othman, N. M. Rasid and W. J. N. Fernando, *Chem. Eng. Sci.*, 2006, **61**, 1555.

29 M. Bouraada, M. Lafjah, M. S. Ouali and L. C. D. Menorval, *J. Hazard. Mater.*, 2008, **153**, 911.

30 (*a*) H. Yin, L. Cui, S. Ai, H. Fan and L. Zhu, *Electrochim. Acta*, 2010, **55**, 603; (*b*) M. J. H. Moreno, M. A. Ulibarri, J. L. Rendon and C. J. Serna, *Phys. Chem. Miner.*, 1985, **12**, 34.

31 C. Forano, T. Hibino, F. Leroux, and C. Taviot-Guého, *Handbook of Clay Science*, 2006, pp. 1021–1095.

32 M. Wendt, L. K. Mahnke, N. Heidenreich and W. Bensch, *Eur. J. Inorg. Chem.*, 2016, **34**, 5393.

33 A. P. Tathod and O. M. Gazit, *Cryst. Growth Des.*, 2016, **16**, 6709.

34 J. Stetefeld, S. A. McKenna and T. R. Patel, *Biophys. Rev.*, 2016, **8**, 409.

35 (*a*) P. Cruz, F. Rocha and A. Ferreira, *CrystEngComm*, 2016, **18**, 9113; (*b*) J. MCGinty, N. Yazdanpanah, C. Price, J. H. T. Horst, and J. Sefcik, *Handbook of Continuous Crystallization*, RSC Publishing, 2020, pp. 1–53, ISBN 978-1-78801-214-0.